Geoscientific
Model Development
Discussions

Open Access

Representation of climate extreme indices in the coupled atmosphere-land surface model ACCESS1.3b

R. Lorenz[1], A. J. Pitman[1], M. G. Donat[1], A. L. Hirsch[1], J. Kala[1], E. A. Kowalczyk[2], R. M. Law[2], and J. Srbinovsky[2]

[1]ARC Centre of Excellence for Climate System Science and Climate Change Research Centre, University of New South Wales, Sydney NSW 2052, Australia
[2]Centre for Australian Weather and Climate Research, CSIRO Marine and Atmospheric Research, Aspendale VIC 3195, Australia

Correspondence to: R. Lorenz (r.lorenz@unsw.edu.au)

GMDD

6, 6343–6389, 2013

Climate extremes in ACCESS1.3b

R. Lorenz et al.

Printer-friendly Version

Interactive Discussion

Printer-friendly Version

Interactive Discussion

Abstract

Climate extremes, such as heat waves and heavy precipitation events, have large impacts on ecosystems and societies. Climate models provide useful tools to study underlying processes and amplifying effects associated with extremes. The Australian Community Climate and Earth System Simulator (ACCESS) has recently been coupled to the Community Atmosphere Biosphere Land Exchange model. We examine how this model represents climate extremes derived by the Expert Team on Climate Change Detection and Indices and compare them to observational datasets using the AMIP framework. We find that the patterns of extreme indices are generally well represented. Indices based on percentiles are particularly well represented and capture the trends over the last 60 yr shown by the observations remarkably well. The diurnal temperature range is underestimated, minimum temperatures (T_{MIN}) during nights are generally too warm and daily maximum temperatures (T_{MAX}) too low in the model. The number of consecutive wet days is overestimated while consecutive dry days are underestimated. The maximum consecutive 1 day precipitation amount is underestimated on the global scale. Biases in T_{MIN} correlate well with biases in incoming longwave radiation, suggesting a relationship with biases in cloud cover. Biases in T_{MAX} depend on biases in net shortwave radiation as well as evapotranspiration. The regions and season where the bias in evapotranspiration plays a role for the T_{MAX} bias correspond to regions and seasons where soil moisture availability is limited. Our analysis provides the foundation for future experiments that will examine how land surface processes contribute to these systematic biases in the ACCESS modelling system.

1 Introduction

Climate extremes, including heat waves, heavy precipitation events or droughts have important effects on ecosystems and society (Easterling, 2000; Ciais et al., 2005; Pall et al., 2011). Many climate extremes are related to natural variability (Arblaster and

Alexander, 2012; Seneviratne et al., 2012). However, climate change has the ability to modify the frequency, intensity, spatial extent, duration, and timing of climate extremes, and can lead to events unprecedented in the historical record (Seneviratne et al., 2012). Given the impact of extremes, it is important to understand their causes, how

5 they might change in the future and the role of potential interacting processes and feedbacks that might amplify them. This is urgent given some extremes appear to be increasing in frequency (Alexander et al., 2006; Coumou and Rahmstorf, 2012; Donat and Alexander, 2012; Perkins et al., 2012) and that extremes are considered to be a particularly challenging aspect of climate change adaptation (IPCC, 2012).

10 Extreme events can be directly influenced by land surface processes. Heat waves for example can be amplified by land surface processes including dryness and decreased vegetation (Zaitchik et al., 2006; Fischer et al., 2007; Koster et al., 2009; Hirschi et al., 2010; Stéfanon et al., 2012; Lorenz et al., 2013). Limited soil moisture availability and less active vegetation decreases evapotranspiration and, therefore, more energy is

15 available for the sensible heat flux which increases temperatures (e.g., Seneviratne et al., 2010). Temperature variability is also affected by land surface processes (Seneviratne et al., 2006) and Jaeger and Seneviratne (2010) found a tendency for a greater impact of land surface processes on maximum temperatures, as distinct from minimum temperatures. The land–atmosphere coupling mechanisms for maximum and

20 minimum temperatures differ. A clear relationship between maximum temperature and realistic soil moisture initialisation was found by Hirsch et al. (2013). This is in contrast to minimum temperatures where the influence of soil moisture is less clear given the role of net long wave emission in modulating nighttime temperatures. Interactions between the land surface and precipitation also exist, but the scale of the impact is

25 less clear. It remains uncertain how soil moisture affects rainfall, with no agreement on the sign of the feedback (Findell and Eltahir, 2003; Ek and Holtslag, 2004; Taylor and Ellis, 2006). Pitman et al. (2012) analysed several global climate models to examine the impact of land use changes on temperature and precipitation extremes and found opposing effects to the impact of increasing CO_2 for some extreme indices and additive

impacts for others. In short, to understand the changes in extremes linked with natural variability or increasing CO_2 we need to understand how land surface processes influence climate extremes.

Land–atmosphere feedbacks are difficult to investigate using observations alone because of the lack of suitable long-term datasets and the uncertainty regarding how feedbacks might change in the future with climate change. Climate models are useful tools to investigate land–atmosphere feedbacks and their influence on extreme events (Fischer et al., 2007; Jaeger and Seneviratne, 2010; Lorenz et al., 2010). In Australia, a new global earth system model (ACCESS) has been developed (Bi et al., 2013; Kowalczyk et al., 2013). ACCESS1.0 compares well with other models in the Coupled Model Intercomparison Project, version 5 (CMIP-5) with regards to the representation of extremes (Sillmann et al., 2013). A more recent version of the model, ACCESS1.3, has also been used to run CMIP-5 simulations and performs similarly to ACCESS1.0 (Kowalczyk et al., 2013). Two major differences between ACCESS1.0 and ACCESS1.3 are the parameterization of the land surface and the cloud scheme. In ACCESS 1.0, the UK Meteorological Office Surface Exchange Scheme (MOSES) is used, but is replaced in ACCESS1.3 by the Community Atmosphere Biosphere Land Exchange (CABLE1.8) model. The two versions of the model were compared by Kowalczyk et al. (2013) although this analysis did not examine the representation of extreme events.

In this study, we undertake an analysis of the ACCESS1.3 model in terms of its ability to simulate a selection of extremes. We use ACCESS1.3, but replace CABLE1.8 with CABLE2.0 (the most recent released version) in an overall modelling system labelled ACCESS1.3b. We use an Atmospheric Model Intercomparison Project (AMIP) style experimental design (Gates, 1992) involving simulations over the period 1950–2012 with prescribed sea surface temperatures and sea ice concentration. The use of the AMIP experimental design decreases the uncertainty in terms of sea surface temperatures and associated teleconnections including the El Niño-Southern Oscillation. Our analysis focuses on the simulation of climate extreme indices defined by the Expert Team on Climate Change Detection and Indices (ETCCDI) which are

provided by two observational datasets by Donat et al. (2013b, a). Our goal is to assess the skill of ACCESS1.3b in simulating extremes and to identify systematic biases, strengths and weaknesses. This provides us with the foundation for future experiments aimed at resolving deficiencies, particularly where these relate to land
5 surface processes. This study is organized as follows: Sect. 2 gives an overview of the model used and the datasets we used for evaluation. Section 3 provides our results. Section 4 provides a discussion and finally Sect. 5 concludes our study.

2 Data and method

2.1 Australian Community Climate and Earth System Simulator (ACCESS1.3b)

10 The Australian Community Climate and Earth System Simulator (ACCESS) has been developed at the Centre for Australian Weather and Climate Research (CAWCR) to provide the Australian climate community with a state-of-the-art fully coupled climate model as well as weather prediction model (Puri et al., 2013). ACCESS1.3b consists of the atmospheric Unified Model (UM7.3, UK Meteorological Office), the
15 Community Atmosphere Biosphere Land Exchange land surface model (CABLE2.0, CSIRO), the Modular Ocean Model (NOAA/GFDL), the Los Alamos sea ice model CICE (LANL) and the coupling framework OASIS (CERFACS) which couples the ocean and sea ice to the atmosphere (Bi et al., 2013). We use ACCESS1.3b in an AMIP-style configuration with prescribed sea surface temperatures and sea ice fractions.
20 These were sourced from the Program for Climate Model Diagnosis and Comparison (Taylor et al., 2000, http://www-pcmdi.llnl.gov/projects/amip/AMIP2EXPDSN/BCS/amipbc_dwnld.php) and regridded and converted to the UM's data format at the UK Meteorological Office. We performed simulations at 1.25° latitude by 1.875° longitude resolution (N96 resolution), 38 vertical levels, and a 30 min time step. The simulation
25 covers the period 1950–2012, the first year is used as spin-up period and not included in the analysis. Orography in ACCESS1.3b are derived from the 30" GLOBE dataset

Climate extremes in ACCESS1.3b

R. Lorenz et al.

(GLOBE Task Team and others, 1999). However, since this dataset has deficiencies over Australia (Bi et al., 2013) it is improved for the Australian region using the Geoscience Australia high quality dataset (Hilton et al., 2003).

2.1.1 The atmosphere: Unified Model (HadGEM3)

5 The atmospheric model in ACCESS1.3b is the Unified Model developed at the UK Meteorological Office (Davies et al., 2005; Martin et al., 2006). Atmospheric dynamics in the UM are non-hydrostatic, fully compressible and the advection scheme is semi-lagrangian. The vertical coordinates are height based and follow the terrain and a regular Arakawa C grid is used in the horizontal. The radiation scheme is
10 a general two-stream scheme developed by Edwards and Slingo (1996) but was improved in terms of pressure and temperature scaling. These improvements lead to an enhancement of longwave fluxes through the stratosphere (Hewitt et al., 2011). In addition, the tripleclouds scheme of Shonk and Hogan (2008) was included to improve the representation of horizontal cloud inhomogeneity. Calculation of the
15 radiation scheme is performed eight times per day (every sixth time step, 3 hourly). Convection is parameterized by a modified mass flux scheme based on Gregory and Rowntree (1990). The CAPE (convective available potential energy) closure scheme is based on relative humidity and convective momentum transport is parameterized for shallow and deep convection. The critical water content for precipitation is a function
20 of cloud depth and shallower clouds need higher water content before they start to generate precipitation. For shallow convection the scheme also includes revised parcel perturbations that help to make the vertical fluxes more consistent between the boundary layer and the convection scheme (Hewitt et al., 2011; Bi et al., 2013).

The boundary layer mixing scheme is described in Lock et al. (2000). It represents
25 nonlocal mixing in unstable layers and an explicit entrainment parameterization. The entrainment parameterization has been revised to a smoothed adaptive entrainment, which allows air to be detrained out of the parcel's ascent, maintaining parcel buoyancy. Consequently, the parcels reach higher altitudes in the atmosphere compared to the

original scheme. A "buddy" scheme for coastal grid points has been added. It uses the average wind speed over neighbouring sea points to split the near-surface wind speed into separate components over ocean and land portions of a grid cell (Hewitt et al., 2011).

5   The cloud microphysics scheme contains water vapour, total cloud fraction, cloud liquid water and cloud ice as prognostic variables. Precipitation (split into rain, snow and graupel) and cloud phase are prognosed. We use the prognostic condensate scheme PC2 described in Wilson et al. (2008) which represents convective and large-scale clouds. Cloud properties are retained from one time step to the next and are advected
10   with the wind.

Atmospheric chemistry includes the aerosols sulphate, soot, biomass, dust (from IGBP soils, although values are very low), sea salt, and biogenic (climatology only) aerosols. Aerosol emissions are prescribed by monthly climatologies, and aerosols can be advected and deposited.

15   **2.1.2 The land surface: Community Atmosphere Biosphere Land Exchange (CABLE2.0)**

Land surface models simulate biogeophysical and biogeochemical processes and handle the exchange of surface fluxes between the land surface and the atmosphere. Since the extremes explored in this paper are intimately associated with how the land
20   surface is parameterized we provide some detail on how CABLE represents terrestrial processes. Further detailed descriptions of CABLE1.4 can be found in Wang et al. (2011) and CABLE1.8 in Kowalczyk et al. (2013).

CABLE consists of three submodels (1) canopy processes, (2) soil and snow, and (3) carbon pool dynamics and soil respiration. Canopy processes are simulated by a one
25   layer two-leaf canopy scheme, distinguishing between sunlit and shaded leaves for the calculation of photosynthesis, stomatal conductance and leaf temperature (Wang and Leuning, 1998). The vegetation is placed above the ground, which allows for aerodynamic and radiative interactions between the ground and the canopy. CABLE

Climate extremes in ACCESS1.3b

R. Lorenz et al.

includes a sub-grid tiling approach at the surface, meaning that several surface types can exist within a grid-cell (ten vegetation types and three non-vegetated types are distinguished, up to five tiles can be used within each grid cell). The soil model has six layers and the Richards equation is solved for soil moisture while soil temperature is calculated from the heat conduction equation. The snow model has three snowpack layers and calculates temperature, density and thickness of the snow. The carbon pool model used is simple, net primary productivity is calculated from the annual carbon assimilation corrected for respiratory losses (carbon fluxes are not assessed in this study). The differences between CABLE1.8 used in Kowalczyk et al. (2013) and CABLE2.0 used here are small. They include bug fixes and updated optical leaf properties (transmission and reflectance) that are better calibrated for the snow-free soil albedo used by ACCESS.

CABLE has been extensively evaluated (Abramowitz et al., 2008; Wang et al., 2011) and an earlier version was used in the Land Use Change IDentification of robust impacts (LUCID) project (Pitman et al., 2009; de Noblet-Ducoudré et al., 2012). Further, Mao et al. (2011) documents the performance of a low-resolution GCM of intermediate complexity, CSIRO Mk3L, coupled to an earlier version of CABLE (version 1.4b) with a focus on terrestrial quantities. This analysis provides strong evidence that the coupled model produces a reasonable large-scale climatology. More recently, Zhang et al. (2013) ran CABLE2.0 offline with GSWP2 (Global Soil Wetness Project) forcing and compared it with other participating land surface models in GSWP and gridded observations. They found that whilst global mean evapotranspiration (ET) simulated by CABLE agreed well with other land surface models and observations, CABLE underestimated ET in the tropics and had significant runoff errors. In addition, CABLE showed a large sensitivity to soil and vegetation parameters in tropical rainforests and mid-latitude forest regions.

Climate extremes in ACCESS1.3b

R. Lorenz et al.

Full Screen / Esc

Printer-friendly Version

Interactive Discussion

2.2 ETCCDI indices and datasets

The Expert Team on Climate Change Detection and Indices (ETCCDI) defined a set of 27 indices calculated from daily maximum and minimum temperature and daily precipitation (http://www.climdex.org/indices.html). These indices were developed to
investigate changes in intensity, duration and frequency of extreme climate events. Most of these indices describe moderate extremes with return periods of a year or shorter. We calculate all indices using freely available software (http://www.climdex.org/climdex_software.html) and compare the indices from our simulations to the HadEX2 dataset (Donat et al., 2013b). Only a subset of indices are analysed in detail (see
Table 1). We chose four indices that examine the frequency of high (warm days TX90p, warm nights TN90p) and low (cool days TX10p, cool nights TN10p) temperature extremes and one temperature index investigates the amplitude between the coldest and hottest temperature per day (diurnal temperature range DTR). Two of the chosen indices examine wet precipitation extremes (maximum 1 day precipitation amount
Rx1day, consecutive wet days CWD) and one index looks at dryness (consecutive dry days CDD). For temperature extremes, we chose mainly indices based on percentiles which are relative to the base period 1961–1990 because they are applicable over all climate zones and show robust trends in observational datasets (Zhang et al., 2011; Donat et al., 2013b). The precipitation indices were chosen to examine several aspects
of precipitation extremes, high precipitation amounts in Rx1day, high precipitation frequency in CWD and low precipitation frequency and drought in CDD.

2.2.1 HadEX2 dataset

The HadEX2 dataset, described in detail by Donat et al. (2013b), contains 17 temperature and 12 precipitation indices. These are derived from daily maximum and
minimum temperature and precipitation observations for the period covering 1901–2010. The indices were calculated for each station and then the monthly and annual indices were interpolated onto a 3.75° longitude × 2.5° latitude grid. Donat et al. (2013b)

derived linear trends from the gridded fields and tested these trends for statistical significance. The high quality in-situ observations were primarily sourced from the European Climate Assessment and Data set (ECA&D) and associated datasets in south-east Asia and Latin America, GHCN-Daily (USA-only), ETCCDI regional
5 workshops and individual researchers. As a result, the spatial availability of HadEX2 data varies with time. Trend estimates can be influenced by the number of stations included in a dataset. To compare time series and trends of model and observations we calculated global averages. We apply a time independent masking of the model data and HadEX2, only including grid points where more than 50 yr of observational
10 data (out of 60) are available. This minimises the deteriorating effect of variable spatial coverage on the trend calculations. The spatial coverage of the Rx1day index is larger in monthly than annual fields because the decorrelation length scale is larger for monthly compared to yearly extreme precipitation indices. To obtain a spatial coverage that is as good as possible, we calculate the annual maximum Rx1day amounts from
15 the maximum of the monthly Rx1day fields provided by HadEX2. This increases data availability in data sparse regions (e.g. tropics), however, it needs to be taken into account that this may include stations which are less representative for a certain grid point. Therefore, grid points around areas with missing data need to be interpreted with care.
20   When comparing models and gridded observational datasets for extremes, it needs to be kept in mind that scaling effects likely play a role. That is, the gridded observational dataset is derived from annual extremes at each station whereas the models represent a grid point average for each day. Therefore, annual maxima from climate models are expected to be lower in intensity, especially for precipitation based
25 indices Kiktev et al. (2003), Tebaldi et al. (2006).

2.2.2 Other datasets

We use the HadGHCND gridded daily temperature dataset (Caesar et al., 2006) derived from near-surface maximum and minimum temperature observations. It covers

Back | Close

Full Screen / Esc

Printer-friendly Version

Interactive Discussion

the period from 1951 to the present on a 2.75° latitude × 3.75° longitude grid. It was designed for the analysis of climate extremes and the evaluation of climate models. Note that the data coverage is varying with time.

We also use the Global Precipitation Climatology Project (GPCP) Version-2 precipitation (http://www.esrl.noaa.gov/psd/data/gridded/data.gpcp.html) dataset. This is derived from a combination of satellite and rain-gauge measurements (Adler et al., 2003). GPCP is available as global, monthly analysis of surface precipitation at 2.5° × 2.5° resolution from 1979 to the present (we use December 1979–November 2012 here). GPCP has been shown to agree well with ground-based observations (Ma et al., 2009; Pfeifroth et al., 2013).

The NASA "Clouds and the Earth's Radiant Energy System" (CERES EBAF Surface Ed2.7) dataset provides satellite-based estimates of surface radiative fluxes. This data set was specifically created for evaluation of climate models (http://ceres-tool.larc.nasa.gov). It includes surface downwelling shortwave and longwave radiation, surface upwelling shortwave and longwave radiation and estimates for clear-sky radiation from 2001 to 2009. Kato et al. (2013) found that the biases over land were, on average, $21.7\,\mathrm{W\,m^{-2}}$ for downward shortwave and $21.0\,\mathrm{W\,m^{-2}}$ for downward longwave radiation. Therefore, biases between $\pm 10\,\mathrm{W\,m^{-2}}$ are not taken into account in our analysis.

Finally, we use the GLEAM (Global Land-surface Evaporation: the Amsterdam Methodology, Miralles et al., 2011) global evapotranspiration (ET) dataset. This is derived from various satellite products within a Priestley–Taylor framework (Priestley and Taylor, 1972). It estimates daily evaporation at a global scale and a 0.25° spatial resolution and is available from 1984 to 2007. GLEAM uses microwave-derived soil moisture, land surface temperature and vegetation density, as well as the detailed estimation of rainfall interception loss. GLEAM has been found to have a low average bias ($< 5\,\%$, Miralles et al., 2011).

Given the sparse coverage and limited availability of flux observations, satellite estimates provide the "next-best approximation". Although these are strictly models, and not true observations, the algorithms are usually constrained by as much

data as possible (e.g., the GLEAM ET product is driven with gridded precipitation observations), and hence, these products have a well-defined accuracy and are, therefore, useful to compare against global climate models (GCMs), which have much larger degrees of freedom. For the calculation of the biases we used the coarsest grid involved, either interpolating the model output to the coarser grid of the observational dataset or interpolating the observations to the model resolution.

3 Results

First we present seasonal averages of daily maximum (T_{MAX}) and minimum (T_{MIN}) temperatures and total precipitation. Daily T_{MAX}, T_{MIN} and total precipitation data form the basis for the calculation of the ETCCDI indices. The seasonal averages are calculated over December-January-February (DJF), March-April-May (MAM), June-July-August (JJA) and September-October-November (SON). Then we present biases in several (annual) ETCCDI indices before investigating the causes of the differences between model and observations.

3.1 Minimum and maximum temperature and total precipitation

We calculate seasonal averages from daily T_{MIN} and T_{MAX} for the period 1951–2011 from ACCESS1.3b (Figs. 1a and 2a) and compare them to gridded observations from HadGHCND (Figs. 1b and 2b). The overall seasonal patterns are reproduced reasonably well by ACCESS. T_{MAX} shows a negative bias in most regions except North America and parts of South-East Europe and Africa in JJA (Fig. 1c) whereas T_{MIN} shows a positive bias almost globally (Fig. 2c), except for the Arctic and Himalayas. Since HadGHCND does not have a complete coverage in all grid boxes over the whole time period we analysed, regional biases can be influenced by temperature trends, e.g. in East Africa where there is only data between $\sim$ 1960 and 1990 (Caesar et al., 2006). The opposing T_{MAX} and T_{MIN} biases commonly lead to a good simulation of the mean

temperature (Kowalczyk et al., 2013, Fig. 10). Only North America and South-East Europe show a positive bias in boreal summer (JJA) in T_{MAX} as well as T_{MIN}, which results in a pronounced positive bias in JJA mean temperature especially in North America (not shown). Positive temperature biases in central Eurasia and North America were also found by Kowalczyk et al. (2013) who linked them to underestimation of precipitation. The North American bias in JJA has been previously associated with an underestimation of clouds in the area by up to 30 % (Franklin et al., 2013). Overall, however, Fig. 1 suggests a cold bias in T_{MAX} in most regions and in most seasons commonly reaching 4 °C and regionally exceeding 7 °C. The key exception to this is in JJA where there is a warm bias in the Northern Hemisphere mid-latitudes of ~ 2 °C, exceeding 5 °C over North America. Figure 2, in contrast, suggests a warm bias of ~ 2 °C in T_{MIN} almost everywhere, exceeding 5 °C over North Asia in DJF, and North America in JJA. Global patterns of total precipitation are well represented in ACCESS1.3b compared to GPCP during the time period 1980–2012 (Fig. 3a and b). ACCESS1.3b tends to overestimate total seasonal precipitation (Fig. 3c) in most regions, although there is a small underestimate over Europe in most seasons. The wet precipitation bias is largest in the tropics (exceeding 5 mm d^{-1}) but elsewhere it is generally small (< 1 mm d^{-1}). A large negative precipitation bias exists in India in JJA and SON where the monsoon is displaced. This bias has previously been reported by Kowalczyk et al. (2013) and Bi et al. (2013).

3.2 ETCCDI indices

Results for ETCCDI indices in ACCESS1.3b are compared to the HadEX2 dataset. Since the indices are calculated for station data in HadEX2 and then gridded, one would expect that model output might appear smoother with less extremes than the observational dataset (Donat et al., 2013b). In particular, one would expect precipitation based extremes estimates calculated from station-based observations to be more intense. However, we did not find a general underestimation of the variability in the extreme indices in the model.

The percentile-based indices are expected not to differ much from HadEX2, since the percentiles are calculated from the model data and are 10 % on average during the base period (1961–1990) per definition. Hence, differences between ACCESS and HadEX2 are mainly driven by different trends and do not depend on biases

5 in absolute values of T_{MAX} and T_{MIN}. The two indices that examine cold extremes, cool nights (TN10p) and cool days (TX10p) are shown in Fig. 4. The ACCESS1.3b model represents the global patterns of both TN10p (Fig. 4e) and TX10p (Fig. 4f) reasonably well. ACCESS1.3b also captures the decreasing trends in TN10p (Fig. 4g) and TX10p (Fig. 4h) over the period 1951 to 2010. ACCESS underestimates the

10 total trend in TN10p because values are underestimated by ∼ 2 % at the beginning of the simulation and the model data show an increasing trend until the 1980s. After ∼ 1980, the trends are captured well such that the model simulates a close value to the observations of ∼ 6 % of days by 2010. The trend in TX10p is similar to TN10p, but differences are smaller between ACCESS and HadEX2. Both show a decrease

15 from ∼ 11 % to 7 % of days. The global patterns in the two indices representing hot extremes (warm nights, TN90p and warm days, TX90p) are also captured well by ACCESS1.3b (Fig. 5). The regional differences for hot extremes are larger than for cold extremes. There is a large overestimate in the occurrence of TN90p in the Southern Hemisphere, particularly over South America but this difference also affects North

20 America, Australia and southern Africa (Fig. 5e). Similar regions are affected by an overestimation of TX90p (Fig. 5f). Despite these regional differences, ACCESS1.3b estimates the global increasing trends in both TN90p (Fig. 5g) and TX90p (Fig. 5h) remarkably well. We note that this might be because data availability in some of the regions with large differences is too low to pass the requirement of 50+ yr of data

25 in HadEX2 to be included in the global average. Also note the close agreement in interannual variability between ACCESS and HadEX2, suggesting a strong influence from sea surface temperatures, which are prescribed here, on hot extremes. The final temperature index is the diurnal temperature range (DTR, Fig. 6). This is simulated poorly by ACCESS1.3b and is globally underestimated by up to 4 °C (Fig. 6c). This

Title Page

Abstract | Introduction

Conclusions | References

Tables | Figures

◄ | ►

◄ | ►

Back | Close

Full Screen / Esc

Printer-friendly Version

Interactive Discussion

result is anticipated given the seasonal overestimation of T_{MIN} and underestimation of T_{MAX}. The underestimation of DTR is shown clearly in the global time series (Fig. 6d). We put this large underestimation into context with CMIP-5 simulations and reanalysis in the discussion in Sect. 4. There is no clear trend in DTR in the model and the trend in HadEX2 is very hard to see because of the scale of the figure. However, DTR decreases from 11.2 to 11 °C in HadEX2 and was shown to have a significant decreasing trend by Donat et al. (2013b) of ~ 0.05 °C decade^{-1}.

The annual maximum consecutive 1 day precipitation (Rx1day) shows both, regions of over and underestimation (Fig. 7). The pronounced underestimation over India is clearly related to the missing monsoon (Fig. 7c). The smaller underestimation in North America is related to the underestimation of summer rainfall. Central Eurasia also shows an underestimation of Rx1day due to the underestimation in total precipitation during summer, autumn and winter. Overall, ACCESS1.3b underestimates Rx1day (Fig. 7d) by ~ 2–5 mm (~ 5–10 %). However, ACCESS1.3b clearly captures some elements of Rx1day and some of the variability between 1951 and 2010. We also analysed Rx5day (maximum annual consecutive 5 day precipitation) that showed an overestimation from ACCESS on global average (not shown). However, this is an artefact of how we calculate these indices in HadEX2, as maxima out of the monthly maxima, which have a better coverage than the annual maximum (see Sect. 2.3) and the lack of observational data in the tropics. This problem is less pronounced for Rx1day, however, biases around the areas with missing values in HadEX2 have to be taken with care. Consecutive wet days (CWD) are clearly overestimated over the Northern Hemisphere (which is where CWD can be derived due to the low coverage in the Southern Hemisphere), while consecutive dry days (CDD) are underestimated (Fig. 8). There is no clear overall trend in the time series of CWD and CDD (Fig. 8g and h). Overall, there is a clear picture of ACCESS1.3b heavily overestimating consecutive wet days, and underestimating consecutive dry days in those regions where the observations are complete enough to derive these indices.

The biases in extreme precipitation indices are largely influenced by the bias in total precipitation in ACCESS1.3b. This is not a surprise; climate models commonly rain too often, but as low intensity precipitation ("drizzle problem", e.g., Dai, 2006). On a global scale, ACCESS1.3b has too many consecutive wet days, so it rains too often, and underestimates consecutive 1 day precipitation.The biggest bias identified is the underestimation of the diurnal temperature range, due to an overestimation of T_{MIN} and an underestimation of T_{MAX}. Therefore, the next section focuses on the distributions of T_{MIN} and T_{MAX}.

3.3 Probability density functions of T_{MAX} and T_{MIN}

The probability density functions (PDFs) of T_{MAX} and T_{MIN} for ACCESS1.3b and the Had-GHCND dataset are shown in Figs. 9 (DJF) and 10 (JJA). We restrict our analysis of the PDFs to four regions with good data coverage in HadGHCND. These regions are defined in Table 2 and correspond to Asia (ASI), Australia (AUS), Europe (EUR) and North America (NAM). The results from the PDFs are summarized in each panel using the skill score defined by Perkins et al. (2007) which measures the overlap of the PDFs (perfect agreement is a skill score of 1.0).

For DJF, the three northern hemispheric regions (ASI, EUR, and NAM) reproduce the PDFs of the observational data set well. In ASI (Fig. 9a), the lower tail of the T_{MAX} distribution is almost perfectly captured. The upper tail is also captured well although there is a small deviation between 10 and 20 °C. In T_{MIN} the upper tail is well reproduced by ACCESS1.3b but the lower tail shows a bias of ~ 5 °C with too frequent T_{MIN} simulated around −20 °C. In NAM (Fig. 9d), the biases are the opposite; the upper tail of T_{MAX} is better captured than the lower tail, while the lower tail of the T_{MIN} distribution is reproduced well. For EUR (Fig. 9c), both T_{MAX} and T_{MIN} distributions only show small deviations from the observations. For AUS (Fig. 9b), the upper tail of T_{MAX} is reasonably captured, but the mean of T_{MAX} is underestimated and the lower tail shows a bias of ~ 5 °C. The lower tail of T_{MIN} in AUS is better captured than the upper tail, but the whole PDF of T_{MIN} is shifted to the right in the model. Overall the PDF for

both T_{MAX} and T_{MIN} are simulated with a skill score exceeding 0.8 for all regions except AUS in DJF. There is a clear problem with the PDF for T_{MAX} in AUS in DJF linked to a large bias associated with the lower tail of the distribution.

In JJA (Fig. 10), AUS (Fig. 10b) reproduces the distributions of T_{MIN} and T_{MAX} better than the Northern Hemispheric regions ASI and NAM. The lower tail of T_{MIN} is almost perfect but the upper tail has a bias of $\sim 5\,°C$. For T_{MAX} the upper tail is reproduced well, but the lower tail is shifted to the left in the model by about $3\,°C$. Overall, however, ACCESS1.3b captures the T_{MIN} and T_{MAX} for AUS in JJA with a skill score exceeding 0.8. The PDFs for the Northern Hemisphere region are less well captured than in DJF (Fig. 10a, c and d) with half the skill scores below 0.8 for these regions. EUR (Fig. 10c) captures the lower tail for T_{MIN} well, but the upper tail is slightly overestimated. For T_{MAX}, the PDF is shifted to the left in the model by $\sim 3\,°C$ and the mean of the distribution is underestimated. However, for EUR the skill scores in JJA are still larger than 0.8. T_{MAX} in ASI (Fig. 10a) shows a similar picture although the biases are larger than in EUR. T_{MIN} is shifted to the right, especially the main peak that is also underestimated leading to a low overall skill score. In NAM (Fig. 10d), only the lower tail of T_{MIN} is reasonably reproduced by the model, the main peak is underestimated and the upper tail shifted to the right by $\sim 5\,°C$. The lower tail for T_{MAX} in NAM in JJA is too low and the upper tail too high in ACCESS1.3b. Generally, the lower tail of T_{MIN} is reproduced better than the upper tail, whereas the upper tail in T_{MAX} is often reproduced better than the lower tail.

4 Discussion

The driver of temperatures at the Earth's surface is the surface radiation balance, but different components of the radiation balance are associated with T_{MIN} and T_{MAX}. The daily minimum temperature, which normally occurs just before sunrise, is mainly determined by long-wave radiation (LW) because there is no short-wave (SW) radiation during the night. The magnitude of incoming LW (LW_{IN}) depends on sky temperature and emissivity and is affected by cloud cover and humidity while outgoing LW depends

on the emissivity and temperature of the Earth's surface. Maximum temperatures during the day are dependent on the incoming solar radiation (SW) and modulated by cloud cover and aerosols. Surface temperatures are also affected by the surface albedo, availability of soil moisture for evapotranspiration and stability conditions of the atmosphere. We examined the biases in net LW and net SW (SW_{NET}) from ACCESS1.3b to explain the biases in temperature. The satellite product CERES is used to estimate the biases in the radiative fluxes which has a well defined level of accuracy. When compared to CERES, ACCESS generally has excess amount of SW absorbed at the surface (Fig. 11a) in all seasons. In the Northern Hemisphere this is small in DJF and largest in JJA where the bias exceeds $50\,W\,m^{-2}$ over Europe and North America. There are other regions with biases exceeding $50\,W\,m^{-2}$ including central Africa, India and the Amazon delta (Fig. 11a). The high bias in SW_{NET} (Fig. 11a) is likely associated with a low cloud bias enabling excessive incoming SW. This is evident in JJA over India where the Indian monsoon is severely under-predicted, see Fig. 3. The bias in net LW is generally negative (Fig. 11b), especially in the arid and semi-arid areas, pointing to either outgoing LW being overestimated or incoming LW being underestimated. Outgoing LW radiation is directly proportional to the surface temperature to the 4th power. In areas with positive biases in T_{MIN} and T_{MAX}, ACCESS overestimates outgoing LW which could explain the negative bias in net LW radiation in central Eurasia and North America in JJA. Overall, the largest errors in SW_{NET} are in JJA in the Northern Hemisphere and India as well as the Amazon delta in SON. While the largest biases in net LW occur in warm seasons in the arid and semi-arid areas of North Africa, central Eurasia, middle east, India, North America and Australia. The biases in LW and SW lead to an overall overestimation of total net radiation in Northern Hemisphere spring and summer and most of the tropics (not shown).

We calculate temporal correlations between the biases in T_{MIN}/T_{MAX} and radiation per season on each longitude/latitude (using the NCL function "escorc") when biases are larger than $\pm 1\,°C$ or $\pm 10\,W\,m^{-2}$ respectively. The bias in T_{MIN} correlates strongly with the bias in incoming LW (Fig. 12a). This provides further evidence to associate

this temperature bias with problems in the ACCESS1.3b simulated cloud cover. The bias in T_{MAX} correlates with the bias in SW_{NET}, but the correlation is weaker than for T_{MIN} and LW_{IN}. For example, regions with large negative biases in T_{MAX} (Fig. 1c) in the Himalayas, Arctic, and southwest South America, which are persistent in all seasons, do not always correspond to a negative bias in SW_{NET} (Fig. 11a). In the Northern Hemisphere summer, correlations between SW_{NET} biases and T_{MAX} biases are strong (Fig. 12b) and usually exceed ~ 0.8. However, in SON and MAM, and in particular in DJF in the Northern Hemisphere the correlation between SW_{NET} biases and T_{MAX} becomes weaker and even negative in some grid points (Fig. 12b). The weaker correlations between SW_{NET} and biases in T_{MAX} (Fig. 12b) points to other factors than atmospheric processes playing a role and these are likely to be linked to land processes.

ACCESS1.3b is generally lacking in its capacity to capture T_{MAX}. This was apparent in Fig. 1c for T_{MAX} and Fig. 6 for DTR. Reflecting on Figs. 9 and 10, the simulation of T_{MAX} was shifted to the left in the ACCESS1.3b model in both DJF and JJA in all four regions. It is noteworthy that the largest biases tended to be at the lower tail of the PDF for T_{MAX} (only in EUR and ASI in DJF this was not true). The most straightforward explanation for this is linked with evapotranspiration. For instance, Watterson (1997) found close spatial correlations between DTR and SW_{NET} minus the evaporative and sensible fluxes, or LW_{NET}. Examining how well a land surface model simulates evapotranspiration is challenging because a bias in this quantity can result from poor forcing (rainfall, SW and LW), poor surface states (soil moisture) or poor parameterization of the relationship between the states and the fluxes. It is also challenging because there are considerable uncertainties in estimates of evapotranspiration from observations-based products. We use GLEAM (see Sect. 2.5) recognising that this product is a model-based estimate of evapotranspiration and that there are likely significant uncertainties associated with the estimates.

Figure 13a shows the simulation of evapotranspiration in ACCESS1.3b compared with GLEAM. There is a systematic bias in simulated evapotranspiration, commonly

reaching $30\,\mathrm{W\,m^{-2}}$ and regionally exceeding $50\,\mathrm{W\,m^{-2}}$. In almost all cases, ACCESS1.3b simulates excess evapotranspiration. This is in contrast to Zhang et al. (2013) who found an underestimation of ET in the tropics in offline CABLE2.0 runs. There are, however, some important exceptions; there is too little evapotranspiration
5　over the Indian subcontinent in JJA and SON linked with the failure of the monsoon in this model. There is also a lack of evapotranspiration over parts of North America, despite the excess SW, in JJA. However, the pattern of excess evapotranspiration shown in Fig. 13a is large-scale and systematic. The patterns of the evapotranspiration biases are dissimilar to the net LW biases (Fig. 11b) and are weakly linked to the
10　biases in SW_{NET} (Fig. 11a). The largest positive ET biases occur in densely forested areas (e.g. tropics) and in the Northern Hemisphere in summer. As shown in Fig. 1c, most of the biases in T_{MAX} are small, or negative except over the mid-latitudes of the Northern Hemisphere in JJA which are closely linked to the negative rainfall bias in the model (Fig. 3c). This general low bias in T_{MAX} could be explained by the
15　excessive evapotranspiration. Figure 13b shows the temporal correlation (calculated as for temperature and radiation using NCL's "escorc") between biases in T_{MAX} and biases in evapotranspiration (or latent heat flux, LH, in $\mathrm{W\,m^{-2}}$). Small biases ($< \pm 1\,^\circ C$ for T_{MAX} and $< \pm 10\,\mathrm{W\,m^{-2}}$ for LH) are masked to focus on the correlation of significant biases. We expect a negative correlation in areas where either evapotranspiration is too
20　low and T_{MAX} is too high or evapotranspiration is too high and T_{MAX} is too low. There are many regions where the biases in LH and T_{MAX} are negatively correlated. These include regions over the mid-latitudes of the Northern Hemisphere in JJA, Eurasia in SON and the Southern Hemisphere in DJF and JJA. There are also large areas where the correlation is positive including the mid-latitudes of the Northern Hemisphere in SON,
25　high latitudes in MAM and south-east Asia in MAM, JJA and SON. Unfortunately, using LH to explain biases in T_{MAX} is limited by major gaps in T_{MAX} observations. Despite this, the regions where the clearest negative correlations are found, and the seasons they occur within are not unexpected. Areas with negative correlations correspond to areas where evapotranspiration is limited by soil moisture availability, areas where the

correlation between T_{MAX} and ET biases is positive relate to areas where ET is limited by radiation/temperature (see Seneviratne et al., 2010; Jung et al., 2010; Wang and Dickinson, 2012). In regions where ET is limited by soil moisture, a high influence from the land surface on temperature is expected due to strong land–atmosphere coupling (e.g., Seneviratne et al., 2010; Mueller and Seneviratne, 2012). These tend to be transitional regions between wet and dry climates during the summer season in both hemispheres. This link between biases and coupling is an area we will persue in the future.

One question might be how the ACCESS1.3b simulation of the ETCCDI indices compares with other models. Our use of AMIP makes a direct comparison with other models infeasible. However, Sillmann et al. (2013) have provided an evaluation of climate extreme indices from CMIP-5 models for the present climate. In addition to HadEX2, they included four reanalysis datasets in their analysis. Some of the reanalysis also show large biases to the observations, partly due to different computational approaches when calculating indices from daily grid-point averages in comparison to grids of station extremes (Donat et al., 2013c). Therefore, biases between reanalyses/model output and observations are expected to some degree because of scaling effects. Sillmann et al. (2013) concluded that CMIP-5 models are generally able to simulate climate extremes and their trend patterns in comparison to HadEX2. The percentile indices TN10p, TX10, TN90p and TX90p compare very well with CMIP-5 since they are calculated relative to their specific PDF, thus insensitive to biases in absolute temperature values. Sillmann et al. (2013) also found that models and reanalyses disagree with HadEX2 for DTR. HadEX2 shows much larger values for DTR than the median of the analysed CMIP-5 models and most reanalyses. The question might arise if the comparison of the models to HadEX2 is fair for DTR. As mentioned in Sect. 2.5, extreme indices derived from model output are expected to be less intense than those derived from station observations. The spatial-scale mismatch between model and HadEX2 probably explains a small part of the bias. However, the spatial mismatch between models and observations plays less a role for

indices based on monthly averages such as DTR. HadGHCND T_{MAX} and T_{MIN} seasonal averages also suggest an underestimation of the DTR. In addition, Lewis and Karoly (2013) also found deficiencies in the CMIP-5 models in simulating trends in DTR. Hence, the underestimation of DTR is a common problem in many climate models

5 although it remains possible that the model derived DTR is not directly comparable with the observed derived value. Rx1day was not considered in Sillmann et al. (2013). For Rx5day, ACCESS1.3b's global mean is higher than the median of the CMIP-5 ensemble investigated by Sillmann et al. (2013), CWD is at the lower end of the CMIP-5 models and CDD is also lower than the CMIP-5 median. ACCESS1.0 was among the

10 models that reproduces most temperature and precipitation indices reasonably well in Sillmann et al. (2013). Therefore, overall, ACCESS1.3b performs comparably to other CMIP-5 models for ETCCDI with some indices simulated particularly well, and others in a more limited way.

5   Conclusions

15 To provide a benchmark for how well the ACCESS1.3b climate model simulates extremes, we undertook an AMIP-style simulation involving simulations over the period 1950–2012 with prescribed sea surface temperatures and sea ice concentration. Our goal was to identify strengths and weaknesses in the ACCESS1.3b modelling system to provide a basis for experiments and model developments to resolve these weaknesses.

20 Our analysis is founded on the capacity of the model to simulate daily T_{MAX}, T_{MIN} and precipitation. From these three variables we calculated climate extremes derived by the Expert Team on Climate Change Detection and Indices (ETCCDI). This work builds on earlier analyses of the mean climate of the ACCESS1.3 model, that included CABLE1.8 rather than CABLE2.0 by Kowalczyk et al. (2013) and Bi et al. (2013).

25 These analyses showed that ACCESS1.3 captured the large-scale mean temperature and precipitation well, and compared favourably with other climate models in CMIP-5. Our analysis highlighted a large (2–6 ˚C) cold bias in the simulation of T_{MAX} in all

Climate extremes in ACCESS1.3b

R. Lorenz et al.

Printer-friendly Version

Interactive Discussion

seasons and in all regions bar North America. We also showed a large positive bias (1–5 °C) in T_{MIN} in all seasons and in all regions. As a consequence, ACCESS1.3b fails to represent the diurnal temperature range well in comparison with the HadEX2 data. However, the model captures patterns in, and trends in, indices for cool nights (TN10p) and cold days (TX10p) extremely well, although there is an overestimation in the change in both indices between ∼ 1975 and 2010. Warm nights (TN90p) and warm days (TX90p) are also captured well. ACCESS1.3b simulates rainfall indices quite variably. Rainfall intensity (Rx1day) is simulated reasonably well but consecutive wet days are badly overestimated and consecutive dry days are badly underestimated in the model. The biases in temperature related indices are very likely associated with a large positive bias in net short wave radiation (Fig. 12a) and a large negative bias in net long wave radiation (Fig. 12b). Some of the precipitation biases are related to the common "drizzle" problem. Our results highlight challenges in simulating climate extremes in climate models, a result previously identified (Kiktev et al., 2003; Kharin et al., 2013; Sillmann et al., 2013). However, our results provide a benchmark from which we will now examine how land processes can be improved to capture these extremes. There are some clear ways forward for improving the model. Some of the biases are likely linked with a bias in simulating evapotranspiration and this will be a priority to resolve. For example, application of the GLACE methodology (Koster et al., 2006), could be used to quantify the degree of land-atmosphere coupling in ACCESS. Other biases might be linked with albedo, especially the correct parameterisation of snow albedo, which is a common challenge in land surface models. It will be more challenging to identify how to improve the cloud climatology but by identifying these biases, and the impact these have on extreme indices we provide a clear statement of the state of ACCESS1.3b and a benchmark from which the model can be improved.

References

Abramowitz, G., Leuning, R., Clark, M., and Pitman, A.: Evaluating the performance of land surface models, J. Climate, 21, 5468–5481, doi:10.1175/2008JCLI2378.1, 2008. 6350

Adler, R., Huffmann, G., Chang, A., Ferraro, R., Xie, P.-P., Janowiak, J., Rudolf, B., Schneider, U., Curtis, S., Bolvin, D., Gruber, A., Susskind, J., Arkin, P., and Nelkin, E.: The version-2 Global Precipitation Climatology Project (GPCP) monthly precipitation analysis (1979–present), J. Hydrometeorol., 4, 1147–1167, 2003. 6353

Alexander, L. V., Zhang, X., Peterson, T. C., Caesar, J., Gleason, B., Klein Tank, A. M. G., Haylock, M., Collins, D., Trewin, B., Rahimzadeh, F., Tagipour, A., Rupa Kumar, K., Revadekar, J., Griffiths, G., Vincent, L., Stephenson, D. B., Burn, J., Aguilar, E., Brunet, M., Taylor, M., New, M., Zhai, P., Rusticucci, M., and Vazquez-Aguirre, J. L.: Global observed changes in daily climate extremes of temperature and precipitation, J. Geophys. Res., 111, D05109, doi:10.1029/2005JD006290, 2006. 6345

Arblaster, J. M. and Alexander, L. V.: The impact of the El Niño-Southern Oscillation on maximum temperature extremes, Geophys. Res. Lett., 39, L20702, doi:10.1029/2012GL053409, 2012. 6344

Bi, D., Dix, M., Marsland, S. J., Farrell, S. O., Rashid, H. A., Uotila, P., Hirst, A. C., Kowalczyk, E., Golebiewski, M., Sullivan, A., Yan, H., Hannah, N., Franklin, C., Sun, Z., Vohralik, P., Watterson, I., Zhou, X., Fiedler, R., Collier, M., Ma, Y., Noonan, J., Stevens, L., Uhe, P., Zhu, H., Griffies, S. M., Hill, R., Harris, C., and Puri, K.: The ACCESS coupled model: description, control climate and evaluation, Aust. Meteorol. Oceanogr. J., 63, 9–32, 2013. 6346, 6347, 6348, 6355, 6364

Caesar, J., Alexander, L., and Vose, R.: Large-scale changes in observed daily maximum and minimum temperatures: creation and analysis of a new gridded data set, J. Geophys. Res., 111, D05101, doi:10.1029/2005JD006280, 2006. 6352, 6354

Full Screen / Esc

Printer-friendly Version

Interactive Discussion

Ciais, P., Reichstein, M., Viovy, N., Granier, A., Ogée, J., Allard, V., Aubinet, M., Buchmann, N., Bernhofer, C., Carrara, A., Chevallier, F., De Noblet, N., Friend, A. D., Friedlingstein, P., Grünwald, T., Heinesch, B., Keronen, P., Knohl, A., Krinner, G., Loustau, D., Manca, G., Matteucci, G., Miglietta, F., Ourcival, J. M., Papale, D., Pilegaard, K., Rambal, S., Seufert, G., Soussana, J. F., Sanz, M. J., Schulze, E. D., Vesala, T., and Valentini, R.: Europe-wide reduction in primary productivity caused by the heat and drought in 2003, Nature, 437, 529–533, 2005. 6344

Coumou, D. and Rahmstorf, S.: A decade of weather extremes, Nat. Clim. Change, 2, 491–496, doi:10.1038/nclimate1452, 2012. 6345

Dai, A.: Precipitation characteristics in eighteen coupled climate models, J. Climate, 19, 4605–4630, doi:10.1175/JCLI3884.1, 2006. 6358

Davies, T., Cullen, M. J. P., Malcolm, A. J., Mawson, M. H., Staniforth, A., White, A. A., and Wood, N.: A new dynamical core for the Met Office's global and regional modelling of the atmosphere, Q. J. Roy. Meteor. Soc., 131, 1759–1782, doi:10.1256/qj.04.101, 2005. 6348

de Noblet-Ducoudré, N., Boisier, J.-P., Pitman, A., Bonan, G. B., Brovkin, V., Cruz, F., Delire, C., Gayler, V., van den Hurk, B. J. J. M., Lawrence, P. J., van der Molen, M. K., Müller, C., Reick, C. H., Strengers, B. J., and Voldoire, A.: Determining robust impacts of land-use-induced land cover changes on surface climate over North America and Eurasia: results from the first set of LUCID experiments, J. Climate, 25, 3261–3281, doi:10.1175/JCLI-D-11-00338.1, 2012. 6350

Donat, M. G. and Alexander, L. V.: The shifting probability distribution of global daytime and night-time temperatures, Geophys. Res. Lett., 39, L14707, doi:10.1029/2012GL052459, 2012. 6345

Donat, M., Alexander, L., Yang, H., Durre, I., Vose, R., and Caesar, J.: Global land-based datasets for monitoring climatic extremes, B. Am. Meteorol. Soc., 94, 997–1006, doi:10.1175/BAMS-D-12-00109, 2013a. 6347

Donat, M. G., Alexander, L. V., Yang, H., Durre, I., Vose, R., Dunn, R. J. H., Willett, K. M., Aguilar, E., Brunet, M., Caesar, J., Hewitson, B., Jack, C., Klein Tank, A. M. G., Kruger, A. C., Marengo, J., Peterson, T. C., Renom, M., Oria Rojas, C., Rusticucci, M., Salinger, J., Elrayah, A. S., Sekele, S. S., Srivastava, A. K., Trewin, B., Villarroel, C., Vincent, L. A., Zhai, P., Zhang, X., and Kitching, S.: Updated analyses of temperature and precipitation extreme indices since the beginning of the twentieth century: the HadEX2 dataset, J.

Geophys. Res. Atmos., 118, 2098–2118, doi:10.1002/jgrd.50150, 2013b. 6347, 6351, 6355, 6357

Donat, M. G., Sillmann, J., Wild, S., Alexander, L., Lippmann, T., and Zwiers, F. W.: Consistency of temperature and precipitation extremes across various global gridded, J. Climate, in revision, 2013c. 6363

Easterling, D. R.: Climate extremes: observations, modeling, and impacts, Science, 289, 2068–2074, doi:10.1126/science.289.5487.2068, 2000. 6344

Edwards, J. and Slingo, A.: Studies with a flexible new radiation code, I: Choosing a configuration for a large-scale model, Q. J. Roy. Meteor. Soc., 122, 689–719, 1996. 6348

Ek, M. B. and Holtslag, A. A. M.: Influence of soil moisture on boundary layer cloud development, J. Hydrometeorol., 5, 86–99, doi:10.1175/1525-7541(2004)005<0086:IOSMOB>2.0.CO;2, 2004. 6345

Findell, K. L. and Eltahir, E. A. B.: Atmospheric controls on soil moisture–boundary layer interactions, Part II: Feedbacks within the continental United States, J. Hydrometeorol., 4, 570–583, 2003. 6345

Fischer, E. M., Seneviratne, S. I., Lüthi, D., and Schär, C.: Contribution of land–atmosphere coupling to recent European summer heat waves, Geophys. Res. Lett., 34, L06707, doi:10.1029/2006GL029068, 2007. 6345, 6346

Franklin, C. N., Sun, Z., Bi, D., Dix, M., Yan, H., and Bodas-Salcedo, A.: Evaluation of clouds in ACCESS using the satellite simulator package COSP: regime-sorted tropical cloud properties, J. Geophys. Res.-Atmos., 118, 6663–6679, doi:10.1002/jgrd.50496, 2013. 6355

Gates, W. L.: AMIP: the Atmospheric Model Intercomparison Project, B. Am. Meteorol. Soc., 73, 1962–1970, 1992. 6346

GLOBE Task Team and others: The Global Land One-kilometer Base Elevation (GLOBE) Digital Elevation Model, version 1. Edn., National Oceanic and Atmospheric Administration, National Geophysical Data Center, 325 Broadway, Boulder, Colorado 80305–3328, USA, available at: http://www.ngdc.noaa.gov/mgg/topo/globe.html, last access: 18 November 2013, 1999. 6348

Gregory, D. and Rowntree, P.: A mass flux convection scheme with representation of cloud ensemble characteristics and stability-dependent closure, Mon. Weather Rev., 118, 1483–1506, 1990. 6348

Hewitt, H. T., Copsey, D., Culverwell, I. D., Harris, C. M., Hill, R. S. R., Keen, A. B., McLaren, A. J., and Hunke, E. C.: Design and implementation of the infrastructure of

HadGEM3: the next-generation Met Office climate modelling system, Geosci. Model Dev., 4, 223–253, doi:10.5194/gmd-4-223-2011, 2011. 6348, 6349

Hilton, R. D., Featherstone, W. E., Berry, P. A. M., Johnson, C. P. D., and Kirby, J. F.: Comparison of digital elevation models over Australia and external validation using ERS-1 satellite radar altimetry, Aust. J. Earth Sci., 50, 157–168, doi:10.1046/j.1440-0952.2003.00982.x, 2003. 6348

Hirsch, A. L., Kala, J., Pitman, A. J., Carouge, C., Evans, J. P., Haverd, V., and Mocko, D.: Impact of land surface initialisation approach on sub-seasonal forecast skill: a regional analysis in the Southern Hemisphere, J. Hydrometeorol., in press, doi:10.1175/JHM-D-13-05.1, 2013. 6345

Hirschi, M., Seneviratne, S. I., Alexandrov, V., Boberg, F., Boroneant, C., Christensen, O. B., Formayer, H., Orlowsky, B., and Stepanek, P.: Observational evidence for soil-moisture impact on hot extremes in southeastern Europe, Nat. Geosci., 4, 17–21, doi:10.1038/ngeo1032, 2010. 6345

IPCC: Managing the Risks of Extreme Events and Disasters to Advance Climate Change Adaptation, Cambridge University Press, Cambridge, 2012. 6345

Jaeger, E. B. and Seneviratne, S. I.: Impact of soil moisture–atmosphere coupling on European climate extremes and trends in a regional climate model, Clim. Dynam., 36, 1919–1939, doi:10.1007/s00382-010-0780-8, 2010. 6345, 6346

Jung, M., Reichstein, M., Ciais, P., Seneviratne, S. I., Sheffield, J., Goulden, M. L., Bonan, G., Cescatti, A., Chen, J., de Jeu, R., Dolman, A. J., Eugster, W., Gerten, D., Gianelle, D., Gobron, N., Heinke, J., Kimball, J., Law, B. E., Montagnani, L., Mu, Q., Mueller, B., Oleson, K., Papale, D., Richardson, A. D., Roupsard, O., Running, S., Tomelleri, E., Viovy, N., Weber, U., Williams, C., Wood, E., Zaehle, S., and Zhang, K.: Recent decline in the global land evapotranspiration trend due to limited moisture supply, Nature, 467, 951–954, doi:10.1038/nature09396, 2010. 6363

Kato, S., Loeb, N. G., Rose, F. G., Doelling, D. R., Rutan, D. A., Caldwell, T. E., Yu, L., and Weller, R. A.: Surface irradiances consistent with CERES-derived top-of-atmosphere shortwave and longwave irradiances, J. Climate, 26, 2719–2740, doi:10.1175/JCLI-D-12-00436.1, 2013. 6353

Kharin, V. V., Zwiers, F. W., Zhang, X., and Wehner, M.: Changes in temperature and precipitation extremes in the CMIP5 ensemble, Clim. Change, 119, 345–357, doi:10.1007/s10584-013-0705-8, 2013. 6365

Kiktev, D., Sexton, D. M. H., Alexander, L., and Folland, C. K.: Comparison of modeled and observed trends in indices of daily climate extremes, J. Climate, 16, 3560–3571, 2003. 6352, 6365

Koster, R. D., Sud, Y. C., Guo, Z., Dirmeyer, P. A., Bonan, G., Oleson, K. W., Chan, E., Verseghy, D., Cox, P., Davies, H., Kowalczyk, E., Gordon, C. T., Kanae, S., Lawrence, D., Liu, P., Mocko, D., Lu, C.-H., Mitchell, K., Malyshev, S., McAvaney, B., Oki, T., Yamada, T., Pitman, A., Taylor, C. M., Vasic, R., and Xue, Y.: GLACE: the Global Land–Atmosphere Coupling Experiment, Part I: Overview, J. Hydrometeorol., 7, 590–610, doi:10.1175/JHM510.1, 2006. 6365

Koster, R. D., Schubert, S. D., and Suarez, M. J.: Analyzing the concurrence of meteorological droughts and warm periods, with implications for the determination of evaporative regime, J. Climate, 22, 3331–3341, doi:10.1175/2008JCLI2718.1, 2009. 6345

Kowalczyk, E. A., Stevens, L., Law, R. M., Dix, M., Wang, Y. P., Harman, I. N., Haynes, K., Srbinovsky, J., Pak, B., and Ziehn, T.: The land surface model component of ACCESS: description and impact on the simulated surface climatology, Aust. Meteorol. Oceanogr. J., 63, 65–82, 2013. 6346, 6349, 6350, 6355, 6364

Lewis, S. C. and Karoly, D. J.: Evaluation of historical diurnal temperature range trends in CMIP5 models, J. Climate, 26, 9077–9089, doi:10.1175/JCLI-D-13-00032.1, 2013. 6364

Lock, A. P., Brown, A. R., Bush, M. R., Martin, G. M., and Smith, R. N. B.: A new boundary layer mixing scheme, Part I: Scheme description and single-column model tests, Mon. Weather Rev., 128, 3187–3199, 2000. 6348

Lorenz, R., Jaeger, E. B., and Seneviratne, S. I.: Persistence of heat waves and its link to soil moisture memory, Geophys. Res. Lett., 37, L09703, doi:10.1029/2010GL042764, 2010. 6346

Lorenz, R., Davin, E. L., Lawrence, D. M., Stöckli, R., and Seneviratne, S. I.: How important is vegetation phenology for European climate and heatwaves?, J. Climate, in press, doi:10.1175/JCLI-D-13-00040.1, 2013. 6345

Ma, L., Zhang, T., Frauenfeld, O. W., Ye, B., Yang, D., and Qin, D.: Evaluation of precipitation from the ERA-40, NCEP-1, and NCEP-2 reanalyses and CMAP-1, CMAP-2, and GPCP-2 with ground-based measurements in China, J. Geophys. Res., 114, D09105, doi:10.1029/2008JD011178, 2009. 6353

Mao, J., Phipps, S. J., Pitman, A. J., Wang, Y. P., Abramowitz, G., and Pak, B.: The CSIRO Mk3L climate system model v1.0 coupled to the CABLE land surface scheme v1.4b: evaluation of

Title Page

Abstract | Introduction

Conclusions | References

Tables | Figures

|◄ | ►|

◄ | ►

Back | Close

Full Screen / Esc

Printer-friendly Version

Interactive Discussion

the control climatology, Geosci. Model Dev., 4, 1115–1131, doi:10.5194/gmd-4-1115-2011, 2011. 6350

Martin, G. M., Ringer, M. A., Pope, V. D., Jones, A., Dearden, C., and Hinton, T. J.: The physical properties of the atmosphere in the new Hadley Centre Global Environmental Model (HadGEM1), Part I: Model description and global climatology, J. Climate, 19, 1274–1301, doi:10.1175/JCLI3636.1, 2006. 6348

Miralles, D. G., Holmes, T. R. H., De Jeu, R. A. M., Gash, J. H., Meesters, A. G. C. A., and Dolman, A. J.: Global land-surface evaporation estimated from satellite-based observations, Hydrol. Earth Syst. Sci., 15, 453–469, doi:10.5194/hess-15-453-2011, 2011. 6353

Mueller, B. and Seneviratne, S. I.: Hot days induced by precipitation deficits at the global scale, P. Natl. Acad. Sci. USA, 109, 12398–12403, 2012. 6363

NCL: The NCAR Command Language (Version 6.1.0) [Software], Boulder, Colorado, UCAR/NCAR/CISL/VETS, doi:10.5065/D6WD3XH5, 2013. 6366

Pall, P., Aina, T., Stone, D. A., Stott, P. A., Nozawa, T., Hilberts, A. G. J., Lohmann, D., and Allen, M. R.: Anthropogenic greenhouse gas contribution to flood risk in England and Wales in autumn 2000, Nature, 470, 382–385, doi:10.1038/nature09762, 2011. 6344

Perkins, S. E., Pitman, A. J., Holbrook, N. J., and McAneney, J.: Evaluation of the AR4 climate models' simulated daily maximum temperature, minimum temperature, and precipitation over Australia using probability density functions, J. Climate, 20, 4356–4376, doi:10.1175/JCLI4253.1, 2007. 6358

Perkins, S. E., Alexander, L. V., and Nairn, J. R.: Increasing frequency, intensity and duration of observed global heatwaves and warm spells, Geophys. Res. Lett., 39, L20714, doi:10.1029/2012GL053361, 2012. 6345

Pfeifroth, U., Mueller, R., and Ahrens, B.: Evaluation of satellite-based and reanalysis precipitation data in the tropical Pacific, J. Appl. Meteorol. Clim., 52, 634–644, doi:10.1175/JAMC-D-12-049.1, 2013. 6353

Pitman, A. J., de Noblet-Ducoudré, N., Cruz, F. T., Davin, E. L., Bonan, G. B., Brovkin, V., Claussen, M., Delire, C., Ganzeveld, L., Gayler, V., van den Hurk, B. J. J. M., Lawrence, P. J., van der Molen, M. K., Müller, C., Reick, C. H., Seneviratne, S. I., Strengers, B. J., and Voldoire, A.: Uncertainties in climate responses to past land cover change: first results from the LUCID intercomparison study, Geophys. Res. Lett., 36, L14814, doi:10.1029/2009GL039076, 2009. 6350

Title Page

Abstract | Introduction

Conclusions | References

Tables | Figures

◄ | ►

◄ | ►

Back | Close

Full Screen / Esc

Printer-friendly Version

Interactive Discussion

Pitman, A. J., de Noblet-Ducoudré, N., Avila, F. B., Alexander, L. V., Boisier, J.-P., Brovkin, V., Delire, C., Cruz, F., Donat, M. G., Gayler, V., van den Hurk, B., Reick, C., and Voldoire, A.: Effects of land cover change on temperature and rainfall extremes in multi-model ensemble simulations, Earth Syst. Dynam., 3, 213–231, doi:10.5194/esd-3-213-2012, 2012. 6345

Priestley, C. H. B. and Taylor, R. J.: On the assessment of surface heat flux and evaporation using large-scale parameters, Mon. Weather Rev., 100, 81–92, 1972. 6353

Puri, K., Dietachmayer, G., Steinle, P., Dix, M., Rikus, L., Logan, L., Naughton, M., Tingwell, C., Xiao, Y., Barras, V., Bermous, I., Bowen, R., Deschamps, L., Franklin, C., Fraser, J., Glowacki, T., Harris, B., Lee, J., Le, T., Roff, G., Sulaiman, A., Sims, H., Sun, X., Sun, Z., Zhu, H., Chattopadhyay, M., and Engel, C.: Implementation of the initial ACCESS numerical weather prediction system, Aust. Meteorol. Oceanogr. J., 63, 265–284, 2013. 6347

R: R core Team: a Language and Environment for Statistical Computing, available at: http://www.r-project.org, last access: 18 November 2013, 2013. 6366

Seneviratne, S. I., Lüthi, D., Litschi, M., and Schär, C.: Land–atmosphere coupling and climate change in Europe, Nature, 443, 205–209, 2006. 6345

Seneviratne, S. I., Corti, T., Davin, E. L., Hirschi, M., Jaeger, E. B., Lehner, I., Orlowsky, B., and Teuling, A. J.: Investigating soil moisture–climate interactions in a changing climate: a review, Earth-Sci. Rev., 99, 125–161, 2010. 6345, 6363

Seneviratne, S. I., Nicholls, N., Easterling, D. R., Goodess, C. M., Kanae, S., Kossin, J., Luo, Y., Marengo, J., McInnes, K., Rahimi, M., Reichstein, M., Sorteberg, A., Vera, C., and Zhang, X.: Changes in climate extremes and their impacts on the natural physical environment, in: Manag. Risks Extrem. Events Disasters to Adv. Clim. Chang. Adapt., edited by: Field, C. B., Barros, V., Stock, T. F., Qin, D., Dokken, D. J., Ebi, K. L., Mastrandrea, M. D., Mach, K. J., Plattner, G.-K., Allen, S. K., Tignor, M., and Midgley, P. M., Cambridge University Press, Cambridge, UK, and New York, NY, USA, 109–230, 2012. 6345

Shonk, J. K. P. and Hogan, R. J.: Triplecouds: an efficient method for representing horizontal cloud inhomogeneity in 1-D radiation schemes by using three regions at each height, J. Climate, 21, 2352–2370, doi:10.1175/2007JCLI1940.1, 2008. 6348

Sillmann, J., Kharin, V. V., Zhang, X., Zwiers, F. W., and Bronaugh, D.: Climate extremes indices in the CMIP5 multimodel ensemble: Part 1. Model evaluation in the present climate, J. Geophys. Res.-Atmos., 118, 1716–1733, doi:10.1002/jgrd.50203, 2013. 6346, 6363, 6364, 6365

Stéfanon, M., Drobinski, P., D'Andrea, F., and de Noblet-Ducoudré, N.: Effects of interactive vegetation phenology on the 2003 summer heat waves, J. Geophys. Res., 117, D24103, doi:10.1029/2012JD018187, 2012. 6345

Taylor, C. M. and Ellis, R. J.: Satellite detection of soil moisture impacts on convection at the mesoscale, Geophys. Res. Lett., 33, 11–14, 2006. 6345

Taylor, K. E., Williamson, D., and Zwiers, F.: The Sea Surface Temperature and Sea-Ice Concentration Boundary Conditions For AMIP II Simulations, Tech. rep., Program for Climate Model Diagnosis and Intercomparison (PCMDI), University of California, Lawrence Livermore National Laboratory, Livermore, CA 94550, USA, PCMDI Rep. No. 60, 2000. 6347

Tebaldi, C., Hayhoe, K., Arblaster, J. M., and Meehl, G. A.: Going to the extremes, Clim. Change, 79, 185–211, doi:10.1007/s10584-006-9051-4, 2006. 6352

Wang, K. and Dickinson, R. E.: A review of global terrestrial evapotranspiration: observation, modeling, climatology, and climatic variability, Rev. Geophys., 50, RG2005, doi:10.1029/2011RG000373, 2012. 6363

Wang, Y. and Leuning, R.: A two-leaf model for canopy conductance, photosynthesis and partitioning of available energy, Part I: Model description and comparison with a multi-layered model, Agr. Forest. Meteorol., 91, 89–111, 1998. 6349

Wang, Y. P., Kowalczyk, E., Leuning, R., Abramowitz, G., Raupach, M. R., Pak, B., van Gorsel, E., and Luhar, A.: Diagnosing errors in a land surface model (CABLE) in the time and frequency domains, J. Geophys. Res., 116, G01034, doi:10.1029/2010JG001385, 2011. 6349, 6350

Watterson, I. G.: The diurnal cycle of surface air temperature in simulated present and doubled CO_2 climates, Clim. Dynam., 13, 533–545, doi:10.1007/s003820050181, 1997. 6361

Wilson, D. R., Bushell, A. C., Kerr-Munslow, A. M., Price, J. D., and Morcrette, C. J.: PC2: a prognostic cloud fraction and condensation scheme. I: Scheme description, Q. J. Roy. Meteor. Soc., 134, 2093–2107, doi:10.1002/qj.333, 2008. 6349

Zaitchik, B. F., Macalady, A. K., Bonneau, L. R., and Smith, R. B.: Europe's 2003 heat wave: a satellite view of impacts and land–atmosphere feedbacks, Int. J. Climatol., 26, 743–769, doi:10.1002/joc.1280, 2006. 6345

Zhang, H., Pak, B., Wang, Y. P., Zhou, X., Zhang, Y., and Zhang, L.: Evaluating surface water cycle simulated by the Australian Community Land Surface Model (CABLE) across different spatial and temporal domains, J. Hydrometeorol., 14, 1119–1138, doi:10.1175/JHM-D-12-0123.1, 2013. 6350, 6362

Zhang, X., Alexander, L., Hegerl, G. C., Jones, P., Tank, A. K., Peterson, T. C., Trewin, B., and Zwiers, F. W.: Indices for monitoring changes in extremes based on daily temperature and precipitation data, WIREs Clim. Change, 2, 851–870, doi:10.1002/wcc.147, 2011. 6351

Climate extremes in ACCESS1.3b

R. Lorenz et al.

Back | Close

Full Screen / Esc

Printer-friendly Version

Interactive Discussion

Table 1. Extreme temperature and precipitation indices shown in this study. First 4 indices measure frequency of temperature extremes, DTR measures the amplitude between coldest and hottest daily temperatures and last 3 indices measure rainfall extremes (two wet extremes, last one dry extremes). Percentiles are calculated over reference period 1961–1990.

Index	Indicator name	Definition	Unit
TX10p	Cool days	Percentage of time when daily max temperature < 10th percentile	%
TN10p	Cool nights	Percentage of time when daily min temperature < 10th percentile	%
TX90p	Warm days	Percentage of time when daily max temperature > 90th percentile	%
TN90p	Warm nights	Percentage of time when daily min temperature > 90th percentile	%
DTR	Diurnal temperature range	Annual mean difference between daily max and min temperature	˚C
Rx1day	Max 1 day precipitation	Annual maximum consecutive 1 day precipitation amount	mm
CWD	Consecutive wet days	Maximum number of consecutive days when precipitation ≥ 1 mm	days
CDD	Consecutive dry days	Maximum number of consecutive days when precipitation < 1 mm	days

Table 2. Subregions used for probability density functions

Abbreviation	Name	Definition (Latitude [°], Longitude [°] of region corners)
ASI	Asia	(20° N, 145° E) (20° N, 100° E) (60° N, 100° E) (60° N, 145° E)
AUS	Australia	(50° S, 155° E) (50° S, 110° E) (10° S, 110° E) (10° S, 155° E)
EUR	Europe	(30° N, 75° E) (30° N, 10° W) (70° N, 10° W) (70° N, 75° E)
NAM	North America	(25° N, 60° W) (25° N, 130° W) (60° N, 130° W) (60° N, 60° W)
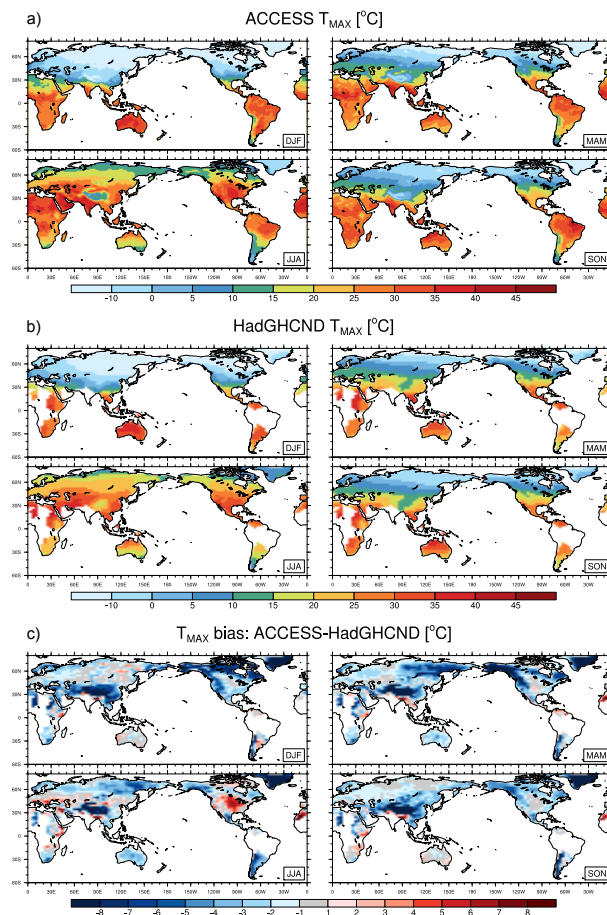
Fig. 1. Daily T_{MAX} for ACCESS1.3b **(a)**, HadGHCND **(b)** and bias **(c)**. Unshaded areas in **(b)** and **(c)** reflect missing observation data. The considered time period is the overlapping time period between model run and observations, 1951–2011.

Title Page

Abstract | Introduction

Conclusions | References

Tables | Figures

◀ | ▶

◀ | ▶

Back | Close

Full Screen / Esc
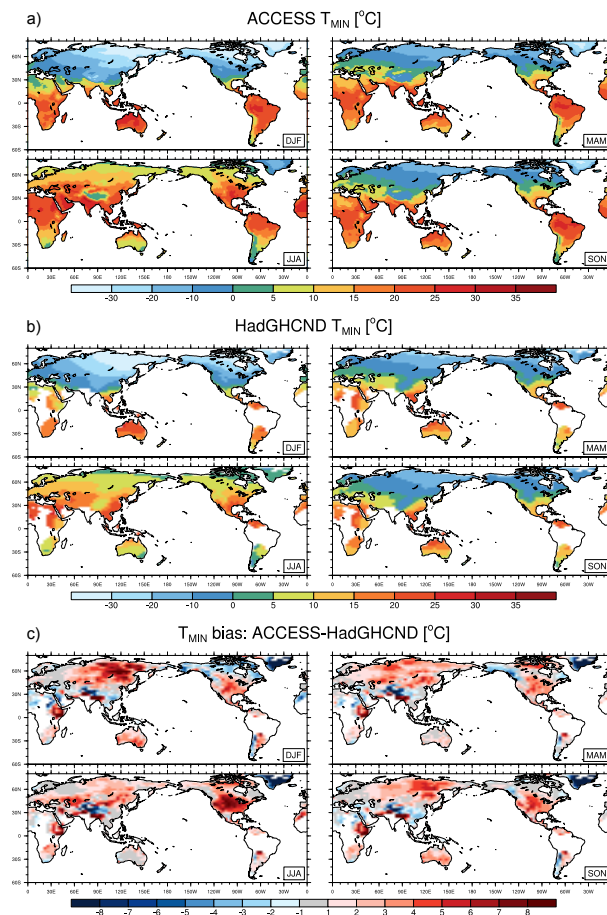
Fig. 2. Daily T_{MIN} for ACCESS1.3b (top row), HadGHCND (middle row) and bias (bottom row). Unshaded areas in **(b)** and **(c)** reflect missing observation data. The considered time period is the overlapping time period between model run and observations, 1951–2011.
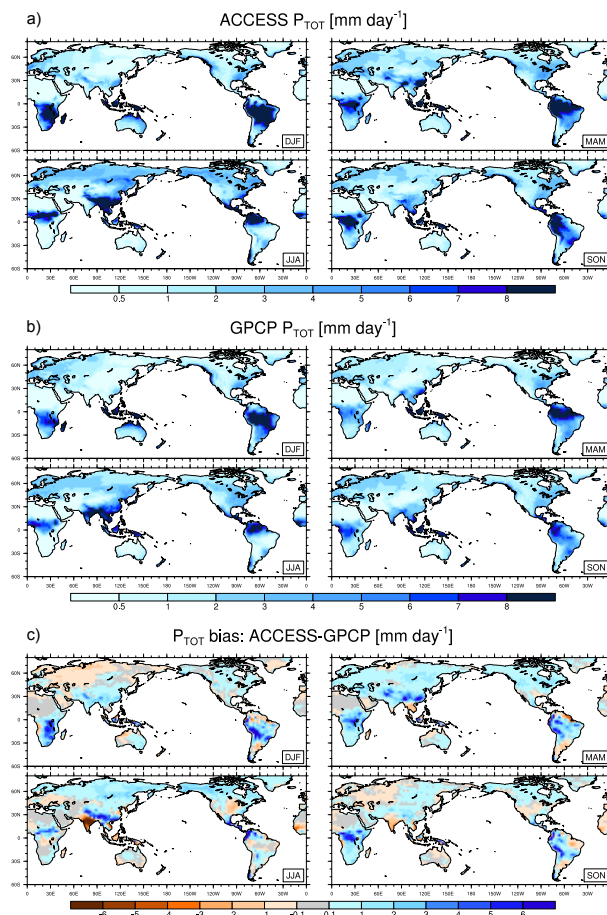
Fig. 3. Total precipitation for ACCESS1.3b **(a)**, GPCP **(b)** and bias **(c)**. The considered time period is the overlapping time period between model run and observations, 1980–2012.
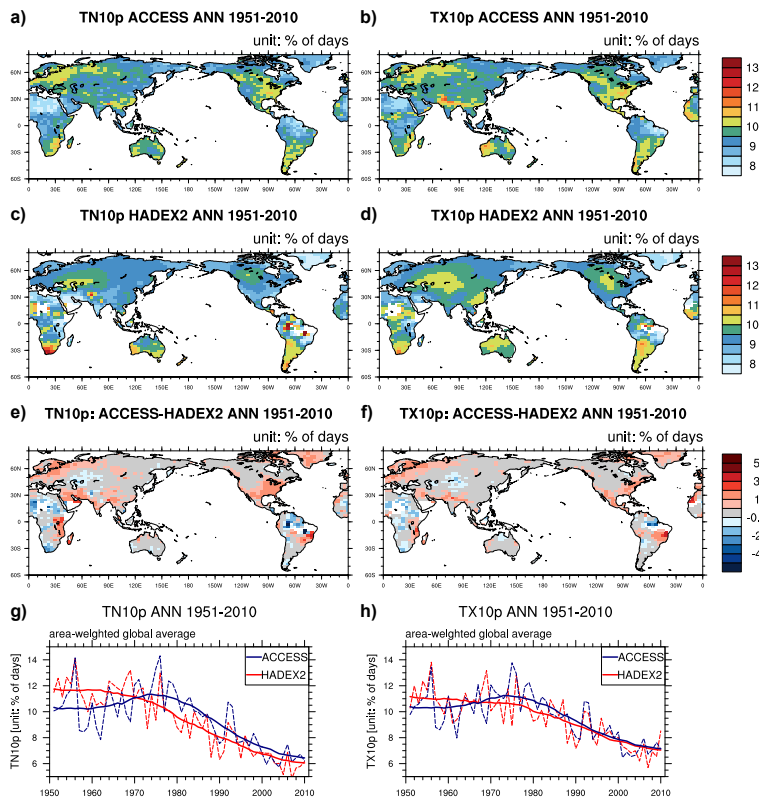
Fig. 4. Annual cool nights (TN10p, left column) and cool days (TX10p, right column) for ACCESS1.3b **(a, b)**, HadEX2 **(c, d)**, bias **(e, f)** and the global average timeseries showing trends **(g, h)**. Unshaded areas reflect missing observation data. ACCESS data were masked depending on the availability of HadEX2 before calcuating the global average. We applied a static masked only including grid point were more than 50 yr of data (out of 60) were available to calculate the global average. The solid lines in panel **(g)** and **(h)** show the timeseries smoothed by a 21 yr gaussian filer while the dashed lines show the yearly values.

Climate extremes in ACCESS1.3b

R. Lorenz et al.

Title Page

Abstract | Introduction

Conclusions | References

Tables | Figures

◄ | ►

◄ | ►

Back | Close

Full Screen / Esc

Printer-friendly Version

Interactive Discussion
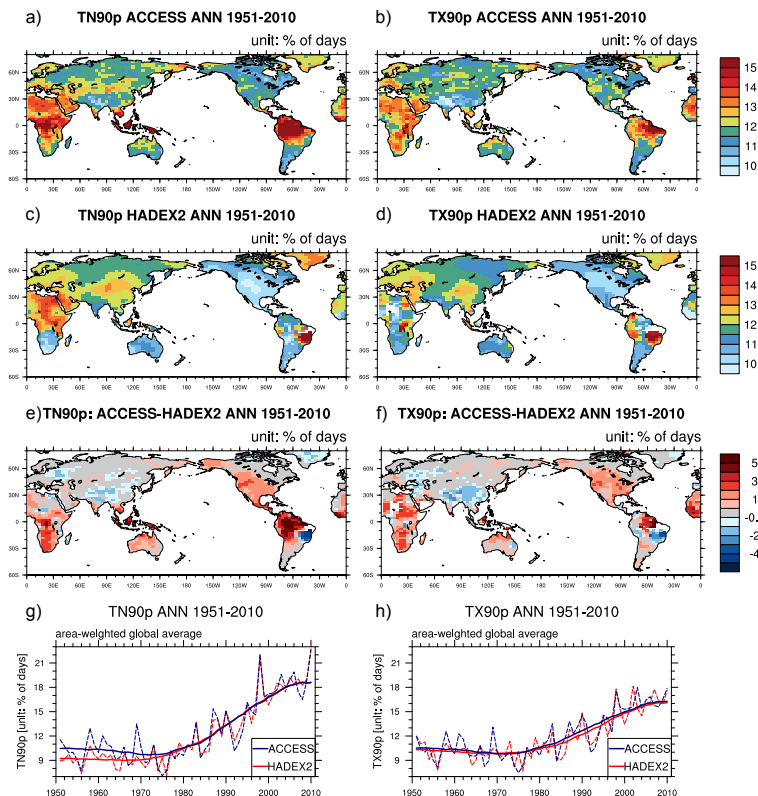
Fig. 5. Annual warm nights (TN90p, left column) and warm days (TX90p, right column) for ACCESS1.3b **(a, b)**, HadEX2 **(c, d)**, bias **(e, f)** and the global average timeseries showing trends **(g, h)**. Unshaded areas reflect missing observation data. We applied a static masked only including grid point were more than 50 yr of data (out of 60) were available to calculate the global average. The solid lines in panel **(g)** and **(h)** show the timeseries smoothed by a 21 yr gaussian filer while the dashed lines show the yearly values.

Title Page

Abstract | Introduction

Conclusions | References

Tables | Figures

|◄ | ►|

◄ | ►

Back | Close

Full Screen / Esc

Printer-friendly Version

Interactive Discussion
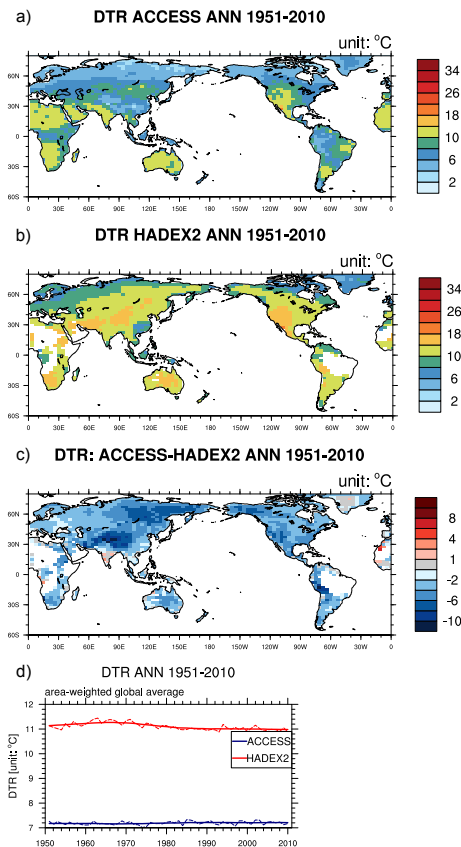
Fig. 6. Annual diurnal temperature range (DTR) for ACCESS1.3b **(a)**, HadEX2 **(b)**, bias **(c)** and the global average timeseries showing trends **(d)**. Unshaded areas reflect missing observation data. We applied a static masked only including grid point were more than 50 yr of data (out of 60) were available to calculate the global average. The solid lines in panel **(g)** show the timeseries smoothed by a 21 yr gaussian filer while the dashed lines show the yearly values.
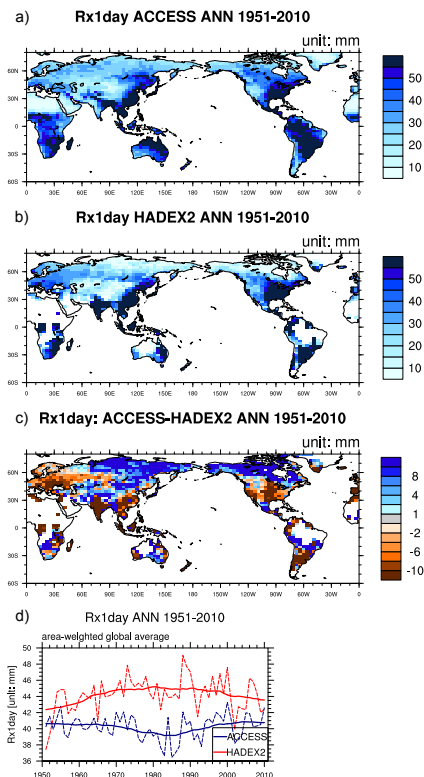
Fig. 7. Annual maximum consective 1 day precipitation (Rx1day) for ACCESS1.3b **(a)**, HadEX2 **(b)**, bias **(c)** and the global average timeseries showing trends **(d)**. Unshaded areas reflect missing observation data. We applied a static masked only including grid point were more than 50 yr of data (out of 60) were available to calculate the global average. The solid lines in panel **(g)** show the timeseries smoothed by a 21 yr gaussian filer while the dashed lines show the yearly values.
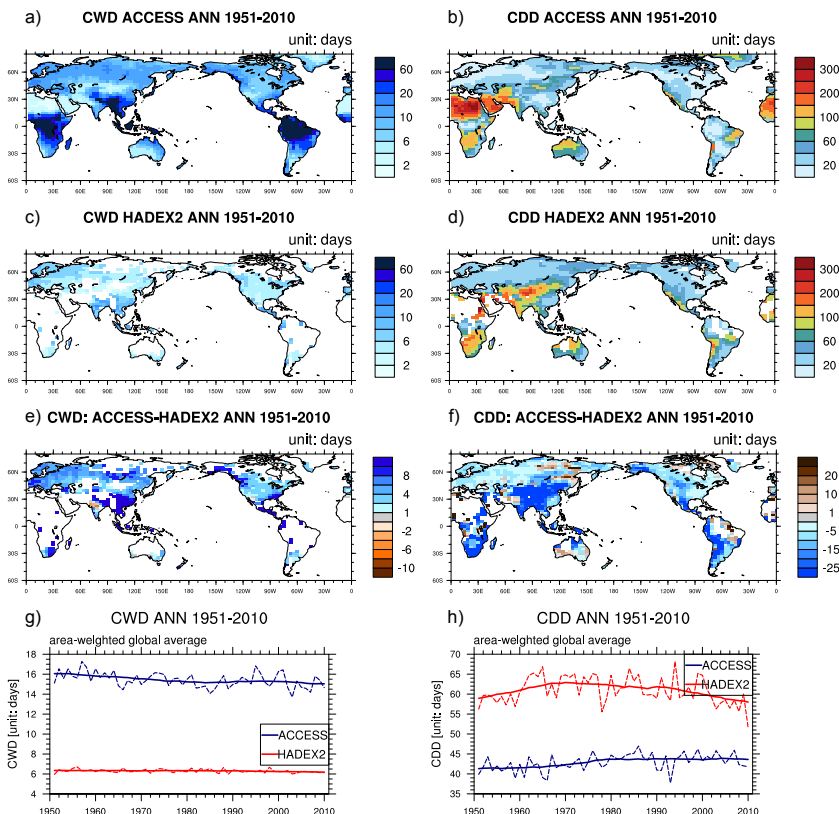
Fig. 8. Annual Consecutive wet days (CWD, left column) and consecutive dry days (CDD, right column) for ACCESS1.3b **(a, b)**, HadEX2 **(c, d)**, bias **(e, f)** and the global average timeseries showing trends **(g, h)**. Unshaded areas reflect missing observation data. We applied a static masked only including grid point were more than 50 yr of data (out of 60) were available to calculate the global average. The solid lines in panel **(g)** and **(h)** show the timeseries smoothed by a 21 yr gaussian filer while the dashed lines show the yearly values.

Title Page

Abstract | Introduction

Conclusions | References

Tables | Figures

◀ | ▶

◀ | ▶

Back | Close

Full Screen / Esc

Printer-friendly Version

Interactive Discussion
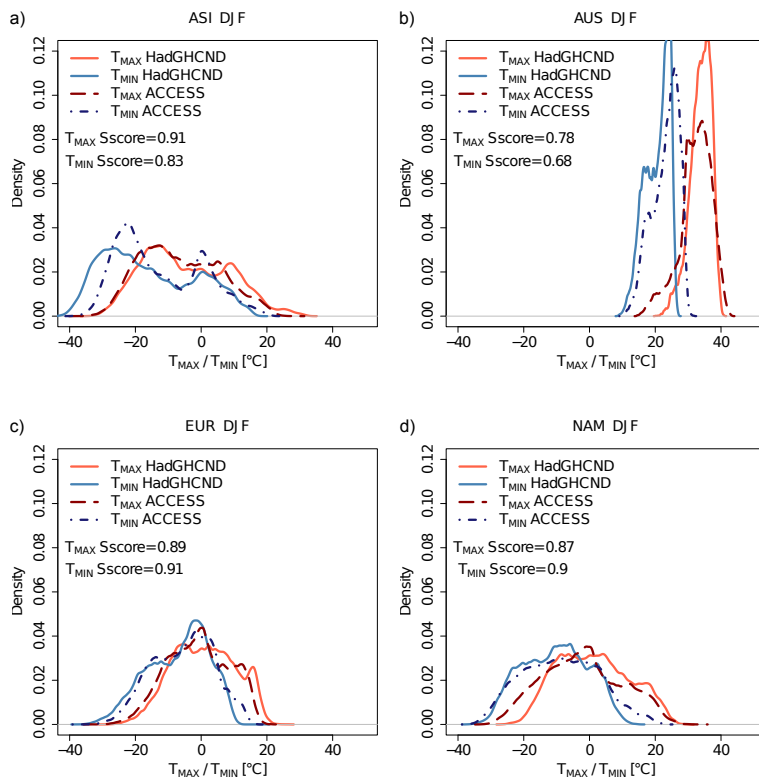
Fig. 9. T_{MAX} and T_{MIN} probability density function for ACCESS1.3b and HadGHCND over Asia, Australia, Europe and North America for DJF (1951–2011) and skill scores for PDFs of T_{MAX} and T_{MIN}. The skill score is calculated by summing up the lower probability at each bin of two given PDFs, $S_{score} = \sum_{1}^{n} minimum(Z_m, Z_o)$ where n is the number of bins used to calculate the PDFs and Z_m and Z_o correspond to the frequency of values in a bin from the model and the observations, respectively.
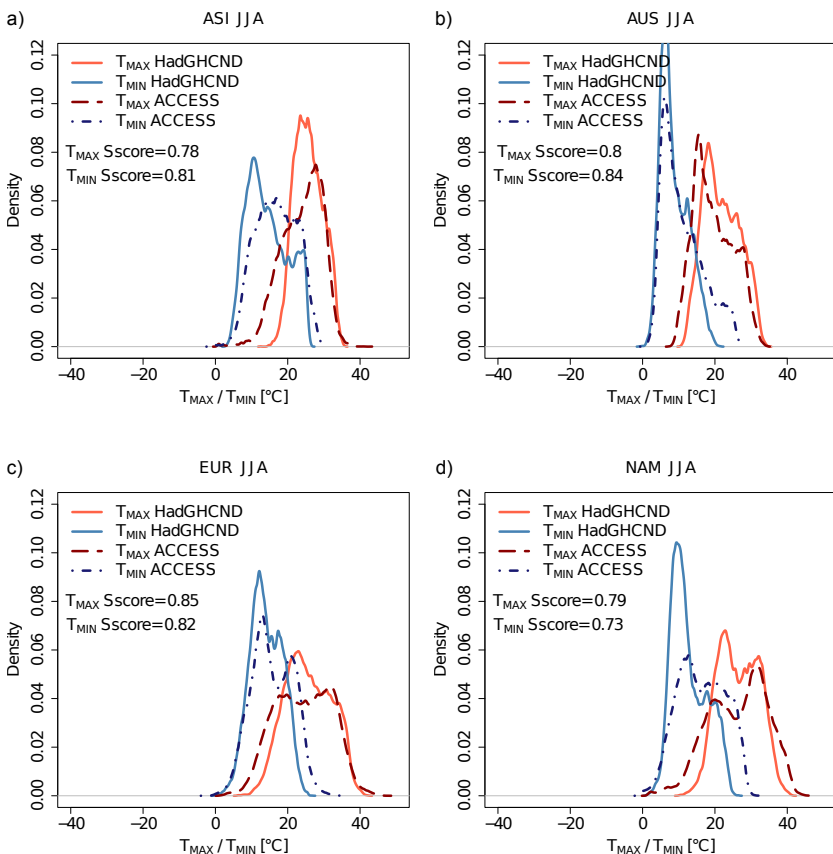
Fig. 10. T_{MAX} and T_{MIN} probability density function for ACCESS1.3b and HadGHCND over Asia, Australia, Europe and North America for JJA (1951–2011) and skill scores for PDFs of T_{MAX} and T_{MIN} (as in Fig. 9).

Climate extremes in ACCESS1.3b

R. Lorenz et al.

Title Page

Abstract | Introduction

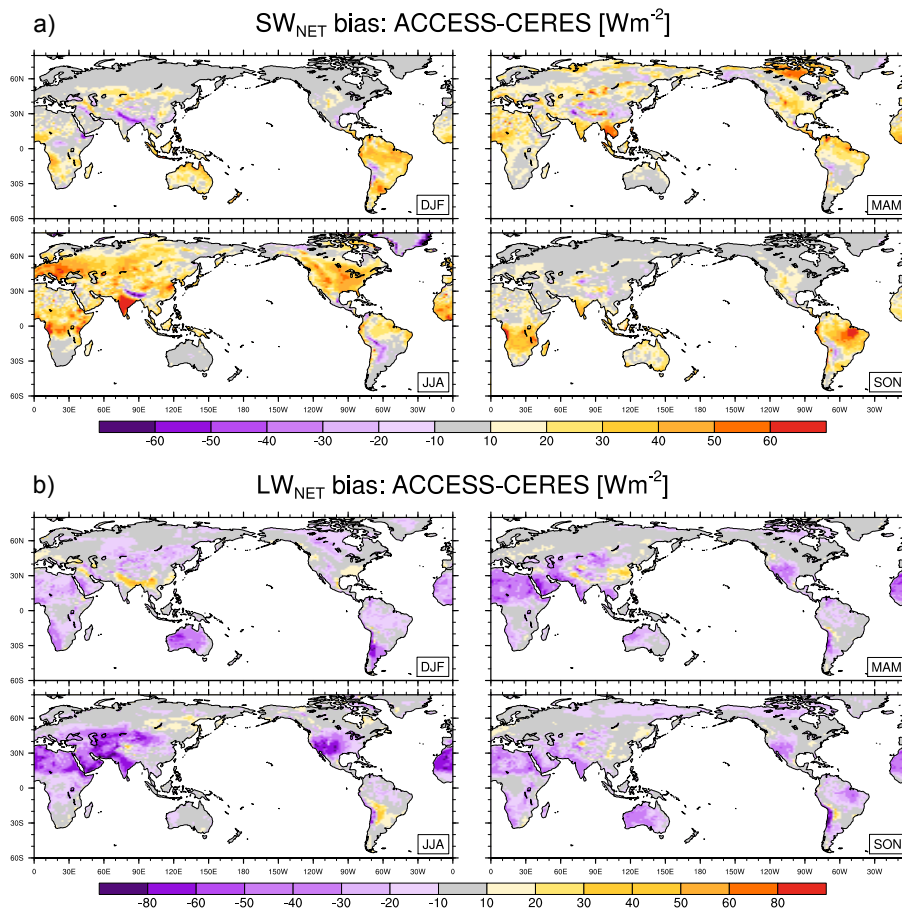Conclusions | References

Tables | Figures

|◄ | ►|

◄ | ►
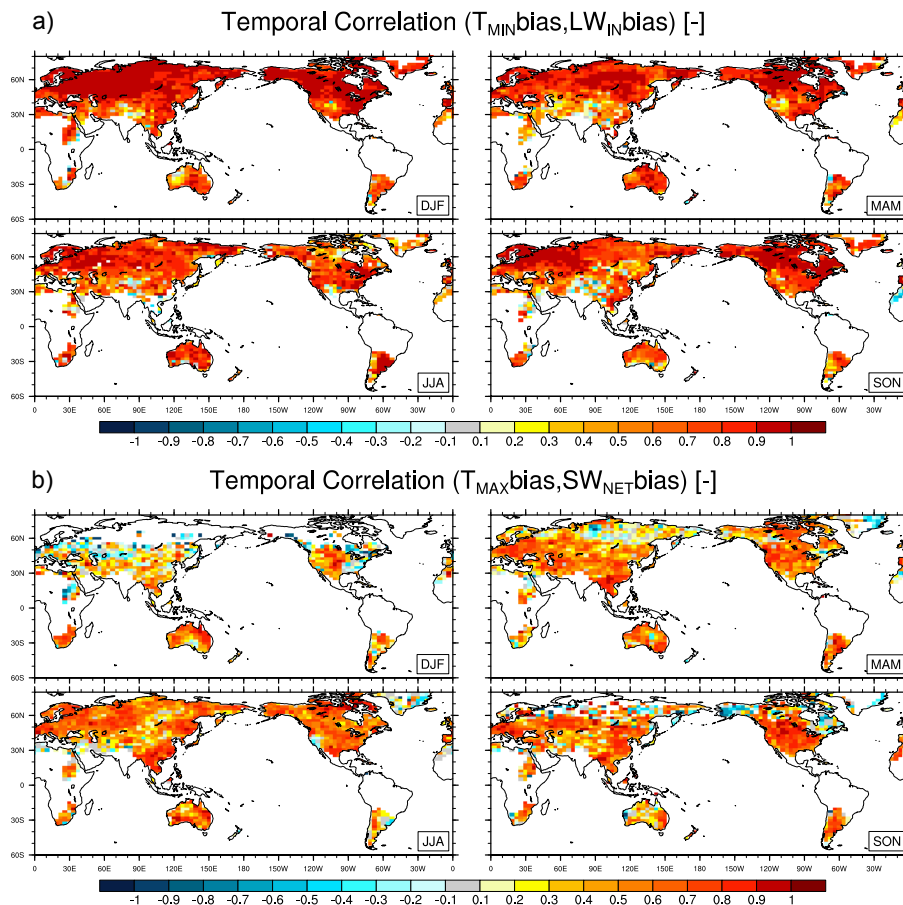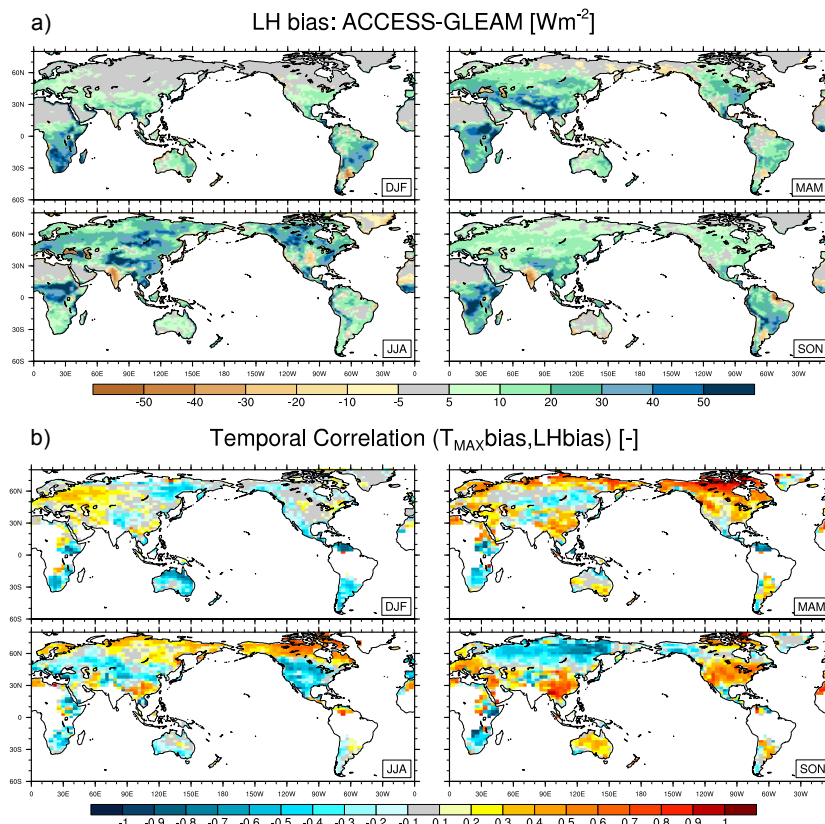
Back | Close

Full Screen / Esc

Printer-friendly Version

Interactive Discussion

Fig. 11. Biases between ACCESS1.3b and CERES in net short-wave radiation **(a)** and net long-wave radiation **(b)**. The considered time period is the overlapping time period between model run and observations, 2001–2009.

Fig. 12. Correlations for biases between ACCESS1.3b and observations in T_{MIN} and LW_{IN} **(a)**, T_{MAX} and SW_{NET} **(b)** in all seasons. Biases smaller than ±1 °C and ±10 W m^{-2} were masked before the calculation of the correlations and are represented by white.

Fig. 13. Biases between ACCESS1.3b and GLEAM data for latent heat flux **(a)** and correlations for biases between ACCESS1.3b and observations in T_{MAX} and LH **(b)** in all seasons. The considered time period is the overlapping time period between model run and observations, 1984–2007. Biases smaller than $\pm 1\,°C$ and $\pm 10\,W\,m^{-2}$ were masked before the calculation of the correlations and are represented by white.

Full Screen / Esc

Printer-friendly Version

Interactive Discussion